THE ASTROPHYSICAL JOURNAL, 404:247–257, 1993 February 10
© 1993. The American Astronomical Society. All rights reserved. Printed in U.S.A.

PIG (PARTIALLY IONIZED GLOBULE) ANATOMY: DENSITY AND TEMPERATURE STRUCTURE OF THE BRIGHT-RIMMED GLOBULE IC 1396E

E. SERABYN,[1] R. GÜSTEN,[2] AND L. MUNDY[3]

Received 1992 March 11; accepted 1992 August 14

ABSTRACT

The bright-rimmed cometary globule IC 1396E, centered roughly on IRAS 21391+5802, has been mapped in a number of molecular transitions in order to determine its density and temperature structure, and to assess the possibility that recent internal star formation was triggered by the ionization front on its southern surface. Based on NH_3 data, gas temperatures in the globule are found to increase outward from the center, from a minimum of $T_k = 17$ K in its tail to a maximum of $T_k = 26$ K on the surface most directly facing the stars ionizing IC 1396. In contrast, the effects of heating by the embedded *IRAS* source are not discernible within the 40″ beam, implying that the bulk of the globule is heated externally.

On the other hand, the density-sensitive CS emission is well correlated with the presence of the embedded *IRAS* source, peaking close to it in the four different rotational transitions observed. The spatial extent of the CS emission decreases with increasing rotational level, indicative of a steep radial density profile. Using a microturbulent radiative transfer code to model the radial dependence of the CS line intensities, and also the intensities of the optically thin $C^{34}S$ $J = 2$–1 and 5–4 lines toward the cloud center, we find a radial density dependence of $r^{-1.55}$ to $r^{-1.75}$ extending out to a sharp cutoff at $r_{\rm max} = 8(\pm 1) \times 10^{17}$ cm^{-2}, beyond which no low-density molecular envelope is present. This $r_{\rm max}$ matches the optical size of the globule very closely. Within $r_{\rm max}$, the globule mass is $480 \pm 120\ M_\odot$.

Because of the observed separation of the density peak from the ionization front, the steep density rise toward the center of the globule must predate the arrival of the ionization front. The high densities ($\langle n \rangle \approx 10^5$ cm^{-3}) and internal turbulent pressures present indicate that the ionization front can have directly compressed only the outermost layers of the cloud, leaving the core density structure relatively unaffected. Thus, the globule had already been evolving toward collapse on its own. While the slight perturbation provided by the added pressure of the ionization front might be sufficient to induce such a core to collapse, spontaneous collapse is the most viable model for the evolution of this globule.

Subject headings: H II regions — ISM: individual (IC 1396E) — ISM: molecules — radio lines: molecular: interstellar — stars: formation

1. INTRODUCTION

The density structure of molecular clouds is of relevance to the star formation process both in terms of the precollapse conditions and also of the ensuing infall phase (Shu 1977; Terebey, Shu, & Cassen 1984; Shu, Adams, & Lizano 1987). Measurement of the density distribution present in a star-forming cloud is best accomplished by comparing the intensities emerging from the cloud in different transitions of a "density-sensitive" molecular species, i.e., one in which excitation is determined by *local* densities through collisions (e.g., Liszt & Leung 1977; Cernicharo 1991). For densities in the range 10^4–10^7 cm^{-3}, a useful molecule in this regard has been CS (Snell, Langer, & Frerking 1982; Snell et al. 1984; Mundy et al. 1986), but only recently, with the advent of large-diameter millimeter- and submillimeter-wave telescopes, has the angular resolution necessary for the study of individual molecular condensations become available (e.g., Schulz et al. 1991; Zhou et al. 1991).

Of particular interest are partially ionized globules (PIGs) found embedded in H II regions, since these molecular condensations are likely the remnants of much more extensive parent molecular clouds which have been dispersed by their stellar offspring (Leung 1985). Hence, such globules tend to be relatively isolated and accessible to direct study. Furthermore, since it has been proposed that star formation in such globules might be induced via compression by external ionization fronts (Nakano et al. 1989; Sugitani et al. 1989; Duvert et al. 1990; Cernicharo et al. 1992), a measurement of such a globule's physical structure (density, temperature, and pressure) could potentially discriminate between spontaneous and stimulated collapse.

The H II region IC 1396 is particularly rich in examples of such globules (Pottasch 1956; Nakano et al. 1989; Sugitani et al. 1989; Duvert et al. 1990; Schwartz, Gyulbudaghian, & Wilking 1991). The PIG associated with bright rim E (Pottasch 1956), centered approximately on IRAS 21391+5802, was selected for study because of the presence of an *IRAS* source and a compact high-velocity molecular outflow (Wilking et al. 1989; Wilking, Blackwell, & Mundy 1990; Sugitani et al. 1989; Walker, Adams, & Lada 1990), both of which are indicative of recent star formation. In addition, the presence of a bright rim on this PIG has already led to the suggestion of radiation-driven implosion (Sugitani et al. 1989).

2. OBSERVATIONS

Figure 1 (Plate 3), an enlargement of an 3AF plate taken as part of the Second Palomer Observatory Sky Survey, shows the bright-rimmed cometary globule IC 1396E and its surroundings. This PIG has been referred to as IC 1396-north

---

[1] California Institute of Technology, Pasadena, CA 91125.

[2] Max-Planck-Institut für Radioastronomie, Auf dem Hügel 69, 5300 Bonn 1, Germany; also California Institute of Technology.

[3] University of Maryland, College Park, MD 20742.

1993ApJ...404..247S

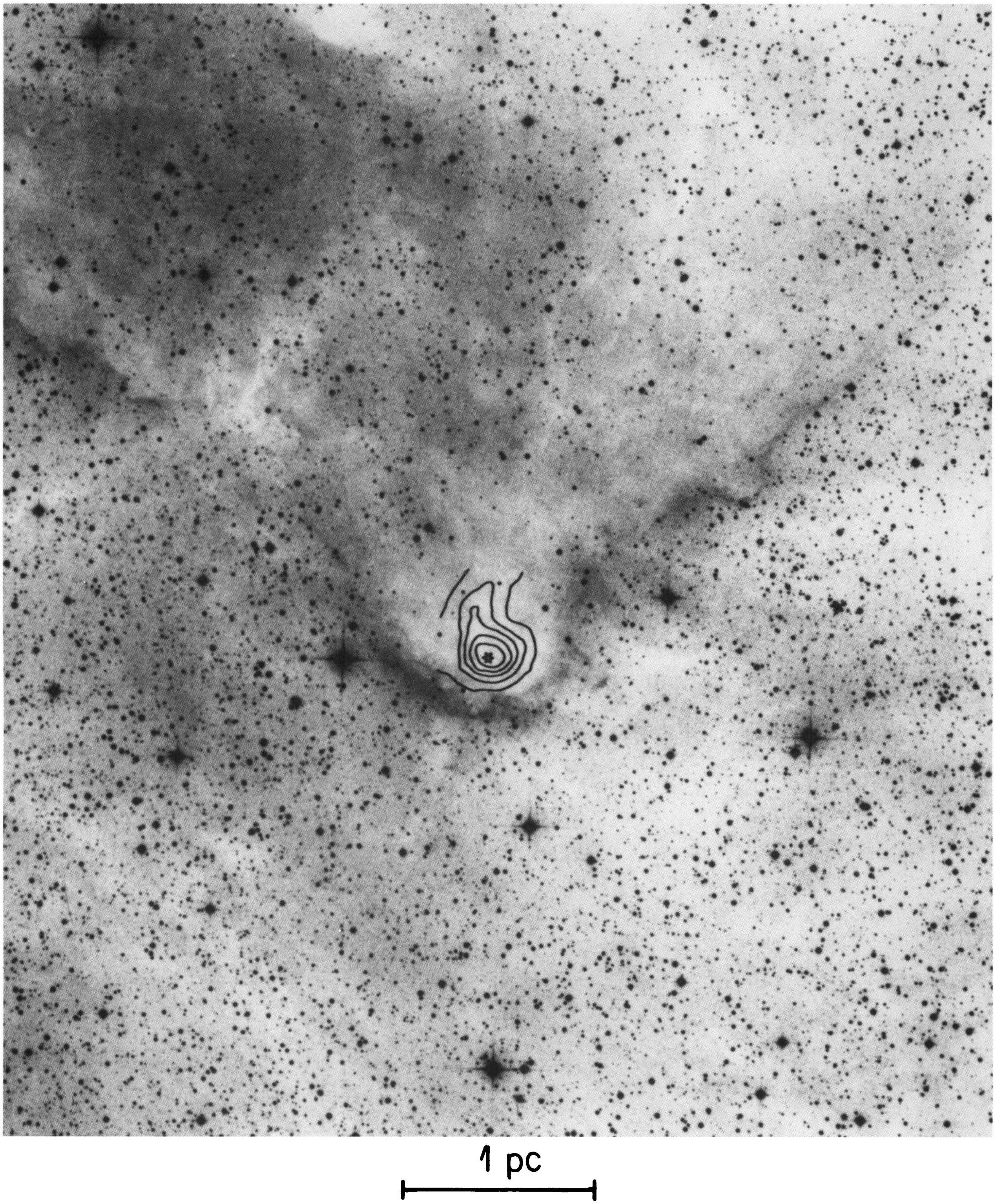

FIG. 1.—Optical (red) photograph of the IC 1396E region, enlarged from the appropriate 3AF plate in the second Palomar Observatory Sky Survey. The star symbol shows the location of IRAS 21391+5802, and the superposed contours show the CS $J = 2$–1 emission integrated over the velocity range 0.75 ± 2 km s^{-1}. The contour levels are 4, 8, 12, 16, and 20 K km s^{-1}. The lowest contour shown is 16% of the peak, implying that the full extent of the CS $J = 2$–1 emission is slightly larger than this contour. The scale at the bottom is for an assumed distance of 750 pc, for which 1 pc = 275″. The reference stars (Table 1) are the three bright stars arranged approximately in a right angle just outside of the ionization front, with the stars located roughly to the east, south, and west of the dark globule.

SERABYN, GÜSTEN, & MUNDY (see 404, 247)

TABLE 1

STELLAR COORDINATES

Source	α_{1950}	δ_{1950}	$\Delta\alpha$	$\Delta\delta$
IRAS 21391+5802....	$21^h39^m10^s.30$	$58°02'29''.0$		
Star W	21 38 39.17	58 04 07.8	$-247''.2$	$98''.8$
Star S....................	21 39 01.17	57 58 38.6	-72.5	-230.4
Star E	21 39 35.88	58 02 15.8	203.1	-13.2

(Sugitani et al. 1989) and GRS 14 (Schwartz et al. 1991), but in keeping with the original nomenclature, we refer to it simply as IC 1396E. Located near the center of the plate, the globule is approximately 0.5–0.6 pc in average diameter, assuming a distance of 750 pc (Matthews 1979). At this distance 1 pc = 275″. The O6 star mainly responsible for ionizing the IC 1396 H II region is one of the components of HD 206267, which lies off the plate at a projected distance of 0°.8 and position angle 195° (e.g., Pottasch 1956; Simonson 1968; Wendker & Baars 1980). The globule and ionization source parameters are summarized in Table 3. In order to correct for unknown projection effects, the ionization source-globule separation listed is the average of the projected distance seen on the sky (10.6 pc), and the maximum radius of the H II region (14.7 pc). The six-pointed star symbol located near the center of the globule in Figure 1 marks the position of IRAS 21391+5802. It was positioned with respect to the three bright stars located just west, east, and south of the globule, which we refer to as W, E, and S, respectively. Their coordinates, accurate to ≈0″.5, were measured with respect to 15 SAO stars on the 3AF plate by N. Reid and are listed in Table 1. The superposed CS contour map will be discussed in § 3.

The globule was mapped in four rotational transitions of CS: the $J = 2$–1 and 3–2 transitions with the IRAM 30 m telescope, and the $J = 5$–4 and 7–6 transitions with the CSO 10.4 m telescope. The beams for all the CS observations were quite similar, 17″–29″ (Table 2). In addition, single spectra of the isotopically substituted $C^{34}S$ $J = 2$–1 and 5–4 transitions were obtained toward the center of the cloud, and the CO $J = 3$–2 line was observed simultaneously with the CS 7–6 line (in the image band). All spectra were calibrated by the standard chopper wheel method. For most lines, the pointing was checked on nearby sources: the continuum radiation from NGC 7027 for the IRAM observations, and the CO 3–2 line in CRL 2688 for the CS 7–6 observations. For these observations, the pointing was accurate to a few arcseconds. However, for the CS $J = 5$–4 observations, the only pointing source available was Saturn, 80° away in declination, implying that the pointing in this line may be less accurate. The globule was also mapped in the NH_3 $(J, K) = (1, 1)$ and (2, 2) inversion transitions with the Effelsberg 100 m telescope, for which the data were calibrated by observation of NGC 7027. All resultant spectra are presented on a main beam temperature, T_{MB}, scale.

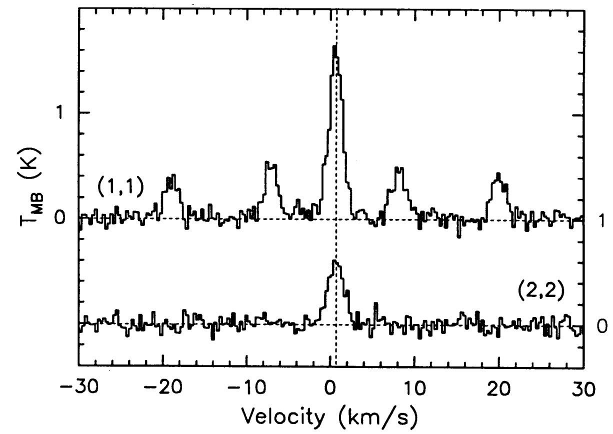

FIG. 2.—NH_3 $(J, K) = (1, 1)$ and (2, 2) spectra observed toward IRAS 21391+5802. The dashed vertical line is at 0.73 km s^{-1}.

The observing parameters, including the observed transitions and frequencies, the telescopes and observation dates, and the beam, receiver, and backend parameters, are summarized in Table 2. The observed positions are indicated in Figures 3*a* and 5, in which the mapping offsets are relative to the nominal coordinates of IRAS 21391+5802 (Table 1). The observing grid for the CS observations was 12″ or 24″, depending on transition, and 20″ for NH_3.

3. NH_3 RESULTS

Figure 2 shows the NH_3 spectra measured toward IRAS 21391+5802. At this location, and over the entire region mapped, the lines are generally weak ($T_{MB} < 2$ K), and, as indicated by the hyperfine component intensity ratios, predominately optically thin ($\tau < 1$ for the central group of hyperfine lines at the T_{MB} maximum). Figure 3*a* shows a map of T_{MB} for the (1, 1) transition integrated over the central group of hyperfine components. The emission follows a narrow north-south ridge ≈150″ long, which for most of its length is unresolved in the E-W direction. However, near its southernmost extremity, the ridge broadens into a cloud with a more NE-SW orientation. The center of this clump is offset from the position of the

TABLE 2

OBSERVING PARAMETERS

Molecular Transition	Frequency (GHz)	Telescope	Observation Date	Beam	Efficiency η_{mb}	Receiver Type	T_{rec}(DSB) (K)	Backend Spectrometer	Resolution (km s^{-1})
NH_3(1, 1)	23.694 495	MPIfR 100 m	1990 July	40″	0.35	Maser	50	Correlator	0.15
NH_3(2, 2)	23.722 633								
$C^{34}S$(2–1)..........	96.412 982	IRAM 30 m	1991 Apr	24	0.63	SIS	120	Filterbank	0.31
CS(2–1)	98.980 968			24	0.63	SIS	120	Correlator	0.12
CS(3–2)	146.969 049			17	0.55	SIS	120	Filterbank	0.20
C^{34}(5–4)	241.016 176	CSO 10.4 m	1990 Aug	29	0.7	SIS	400	Acousto-optical	0.60
CS(5–4)	244.935 606			29	0.7	SIS	400	Acousto-optical	0.59
CS(7–6)	342.882 949			20	0.5	SIS	250	Acousto-optical	0.42
CO(3–2	345.795 975	CSO 10.4 m	1990 Aug	20	0.5	SIS	250	Acousto-optical	0.42

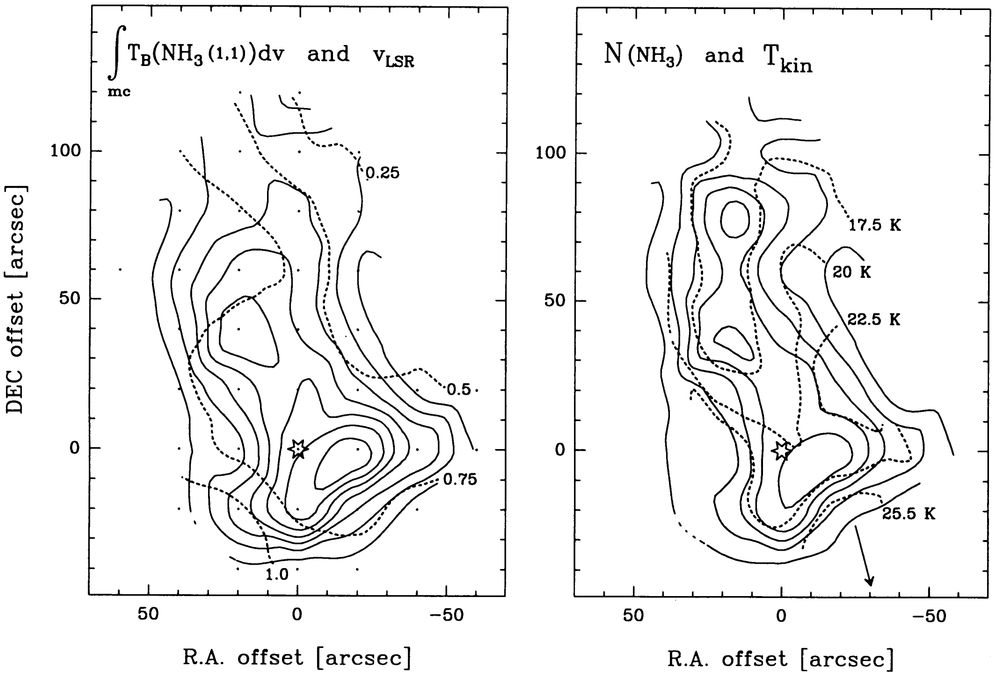

FIG. 3.—NH_3 brightness temperature and column density maps. In both panels the star symbol shows the location of IRAS 21391+5802. (*a*) *Solid contours:* integrated intensity of the main group of hyperfine components of the NH_3 (1, 1) line over the range −1.5 to 2.5 km s^{-1}. The contour levels are 1.2 to 3.6 by 0.4 K km s^{-1}. *Dashed contours:* systemic LSR velocity in units of km s^{-1}. (*b*) *Solid contours:* beam-averaged NH_3 column density. The contour levels are 30, 45, 60, 75, and 90% of the peak level of 3.0×10^{14} cm^{-2}. *Dashed contours:* gas kinetic temperature in K. The arrow points toward HD 206267.

IRAS source by about 15″. Both the southernmost NH_3 clump and the more northerly ridge correspond well with dark regions on the optical photo (Fig. 1), the former with the optically observed globule itself, and the latter with a "tail-like" northward pointing extension to the globule.

Also indicated in Figure 3*a* are the NH_3 systemic LSR velocities, the dashed contours showing a decrease from about 1 km s^{-1} near the southern ionization front to about 0.2 km s^{-1} at the northern extremity of the map, with an average gradient of ≈0.3 km s^{-1} $arcmin^{-1}$. The line width likewise decreases from about 2 km s^{-1} on the southernmost clump to ≈1 km s^{-1} in the north.

3.1. NH_3 *Temperature and Column Density*

Rotation temperatures $T_R(2, 1)$ and NH_3 column densities $N(NH_3)$ were derived from the NH_3 (1, 1) and (2, 2) lines following the procedure described in Pauls et al. (1983). Since the gas kinetic temperature T_K is larger than $T_R(2, 1)$, because of the depopulation of metastable NH_3 levels via collisions, a correction based on statistical equilibrium calculations was applied to the temperatures (Danby et al. 1988). Figure 3*b* shows the resultant $N(NH_3)$ and T_K maps, in solid and dashed contours, respectively.

The column density distribution closely resembles the brightness temperature map of Figure 3*a*. The beam-averaged column density along most of the ridge is rather constant, $2.5 \pm 0.5 \times 10^{14}$ cm^{-2}. The beam-filling factor, η_B, calculated from the ratio of the observed T_{MB} to that expected from the derived rotation temperature and opacity, assuming thermalized populations (Pauls et al. 1983), is also rather constant along the ridge, decreasing from ≈0.5 near the *IRAS* source to ≈0.42 at a location 80″ to the north. This filling factor is largely due to the large-scale coupling of the beam to the globule core and tail, and thus small-scale *area*-filling factors are close to unity. However, although the projected appearance of the cloud must therefore be smooth, this result still allows for the possibility of small-scale clumping with a *volume*-filling factor less than unity.

The kinetic temperature distribution in Figure 3*b* is quite revealing, showing a *minimum* in temperature along the main body of the NH_3 ridge. From this minimum of ≈17 K, the temperature rises toward the eastern, western, and southern cloud edges. The southern clump near the *IRAS* source has a rather uniform temperature of 20–23 K, and the maximum temperature of ≈26 K lies close to the southern ionization front. The uncertainties in these temperatures are ≈1.5 K near the cloud core, and increase to about 3 K near the cloud edges, as the lines get weaker.

Since the highest temperatures lie along the edge of the cloud which faces the ionizing source of the IC 1396 H II region, and there is no noticeable temperature peak at the location of the *IRAS* source, the gas in the bulk of the globule and ridge must evidently be heated externally, by the stellar UV radiation from HD 206267, and not by the embedded *IRAS* source. However, as evidenced by dust continuum emission, the embedded source does heat a small volume in its immediate vicinity (≈7″ diameter; Wilking et al. 1989; Walker et al. 1990), an effect not noticeable in the 40″ NH_3 beam.

4. CS RESULTS

The $C^{32}S$ (hereafter CS) and $C^{34}S$ spectra observed toward IRAS 21391+5802 are shown in Figure 4*a*. The lines consist of a narrow core of roughly 2.5 km s^{-1} FWHM centered at ≈0.73 km s^{-1}, and, in the lines of the CS main isotope, prominent wing emission arising in the molecular outflow. The true width of the line core can be estimated from the optically thin $C^{34}S$ spectra, for which the higher resolution 2–1 spectrum shows a FWHM of 2.3 km s^{-1}. At the central position, the wing emission is seen to be stronger at blueshifted than redshifted velocities, and interestingly, remains strong in even the most highly excited transitions. Even more prominent in the CO $J = 3$–2 spectra, which were acquired simultaneously with the CS 7–6 data, the wing emission extends to quite high velocities, $\approx \pm 40$ km s^{-1} (Fig. 4*b*), much higher than seen in CO $J = 2$–1 (Sugitani et al. 1989).

Maps of the velocity-integrated emission in the four CS lines are shown in Figure 5. In an attempt to separate the line "core" and "wing" emission, two separate velocity intervals are plotted: the maps on the left shows the line core emission (0.75 ± 2 km s^{-1}, a range somewhat wider than the FWHM of the lines in order to allow for spatial velocity shifts), and the maps on the right show the sum of the red and blue wings (-7.25 to -1.25 and 2.75 to 8.75 km s^{-1}). The low signal-to-noise ratio for the wing emission off the central position limits the information available, but the wing emission is evidently more localized than the line core emission.

A comparison of the four line core maps reveals that the line core emission regions decrease markedly in size with increasing rotational level, *J*. Since the observing beams for two of the pairs of transitions are quite similar ($J = 7$–6 vs. 3–2, and $J = 5$–4 vs. 2–1 respectively), this reduction in size with *J* is not resolution-related, but intrinsic to the source. The distributions in the four lines are suggestive of a steep radial density falloff in the globule, as will be elaborated below. However, while three of the transitions in Figure 5 show emission centered directly on IRAS 21391+5802, the 5–4 transition (including the wing map) peaks about 8″–10″ westward. Based on the good agreement of the other three maps, we assume in the following that this anomaly is due to a pointing error, likely the result of the large distance to the pointing source for this one line (§ 2).

The emission in the lower *J* lines of CS are consistent with our NH_3 results. Indeed, an overlay of the CS 2–1 emission contours on the NH_3 column density map (Fig. 6) shows good overall agreement, but some differences in detail. As for NH_3, the CS line shows the emission from the globule centered near IRAS 21391+5802, as well as from the tail extending northward from this globule. However, in CS the contrast between the roundish globule centered on the *IRAS* source and the northerly tail is much greater than in NH_3, and the CS peak is also more directly centered on IRAS 21391+5802. Interestingly, the southernmost NH_3 clump appears more indented in the direction of the exciting O6 star than the CS map, but the NH_3 map is in general less smooth. The line center velocities also agree well, the CS velocities changing very little across the globule in right ascension, but by about 0.3 km s^{-1} $arcmin^{-1}$ with declination. Since this shift is smaller than the observed line width, we attribute the superthermal line width to small-scale turbulence.

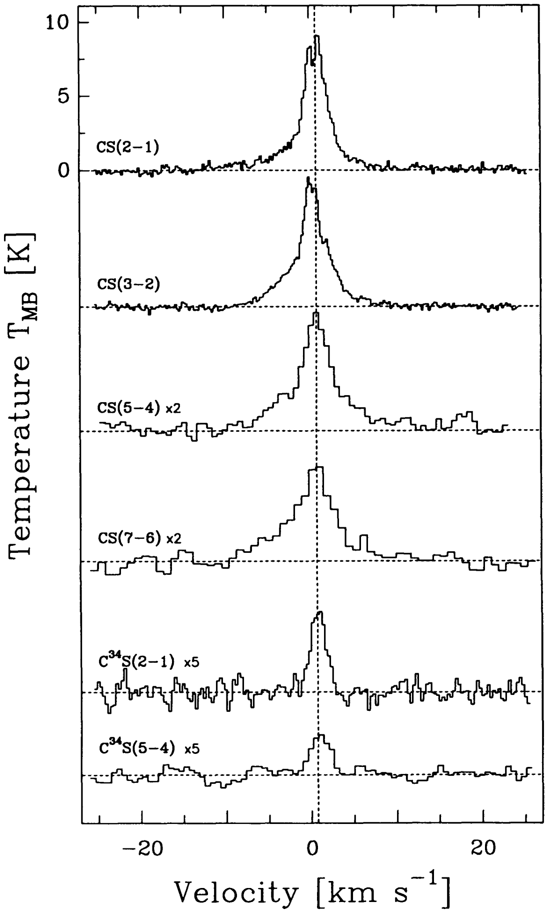

FIG. 4*a*

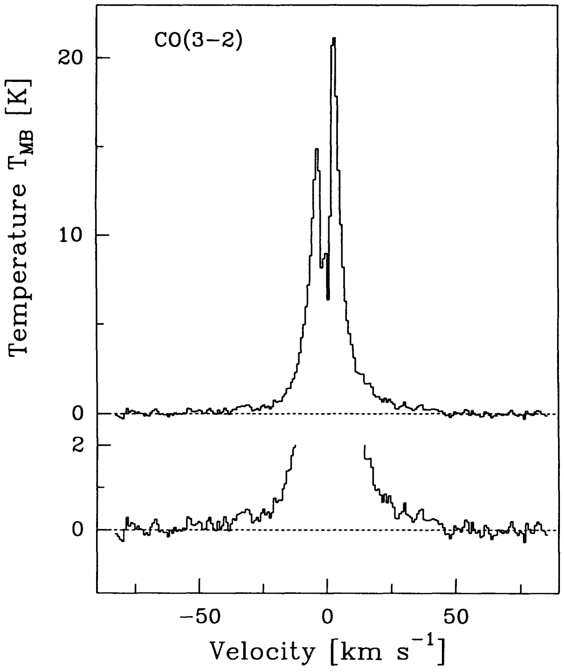

FIG. 4*b*

FIG. 4.—(*a*) CS and $C^{34}S$ spectra toward IRAS 21391+5802. All spectra are presented on the main beam temperature scale, using main beam efficiencies from Table 2. Note the different scales on the spectra. The dashed vertical line is at 0.73 km s^{-1}. (*b*) Average of nine CO 3–2 spectra on a 12″ by 12″ grid centered on IRAS 21391+5802. The bottom spectrum is the same, on an expanded vertical scale.

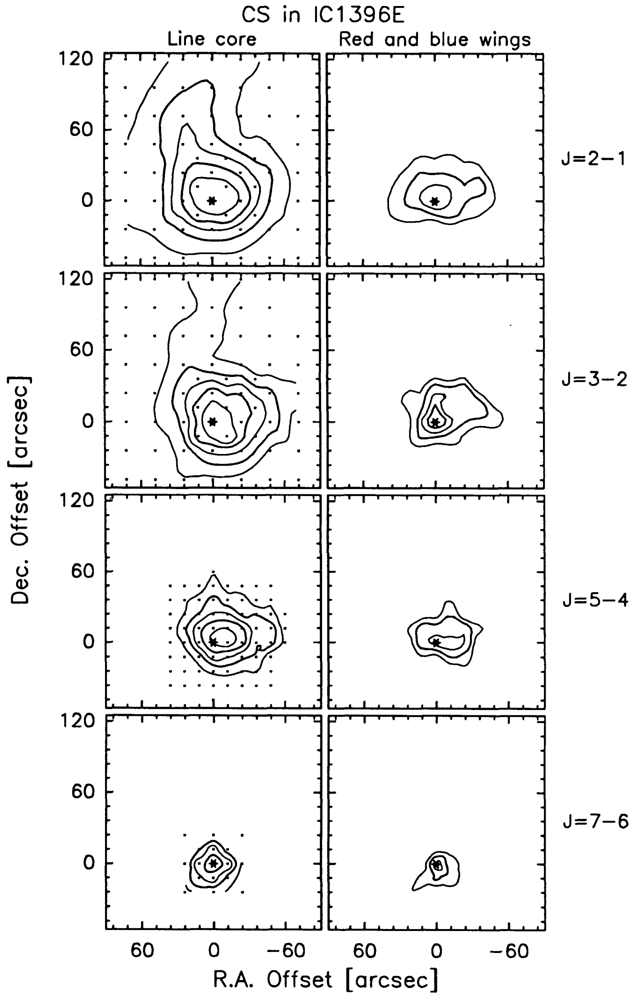

FIG. 5.—Velocity channel maps of integrated CS emission, with observing grids superposed. The star symbol in each panel shows the location of IRAS 21391+5802. From top to bottom, the rows show the $J = 2$–1, 3–2, 5–4, and 7–6 emission. The emission in each line is divided between the line core (0.75 ± 2 km s^{-1}) in the left column, and the sum of the red and blue wings (-7.25 to -1.25 and 2.75 to 8.75 km s^{-1}) on the right. In the line core maps, the levels are 4 to 20 K km s^{-1} by 4 K km s^{-1} for the $J = 2$–1 and 3–2 maps, 2.5 to 12.5 by 2.5 K km s^{-1} for the 5–4 map, and 2 to 8 by 2 K km s^{-1} for the 7–6 map. For all the line wing maps, the contour levels are 3 to 12 K km s^{-1} by 3 K km s^{-1}.

The same CS 2–1 map, but with one lower contour included, is superposed on the optical photo in Figure 1. The lowest contour is 16% of the peak, so the full extent of the emission is slightly larger still. Taking this into account, both the location and size of the CS 2–1 emission region are in good agreement with the globule's optical location and size.

4.1. *Gas Density Profile*

The CS 2–1 and 3–2 emission is composed of a more or less spherical component centered on IRAS 21391+5802 (referred to as the "globule" or the "core" in the following), a weaker "tail" extending northward from this core, and high velocity "line wing" emission localized near IRAS 21391+5802. Separate density estimates were made for all three of these gas components with the aid of radiative transfer codes. Before turning to specific results, we briefly mention various calibration issues (see also the discussions in Snell et al. 1984 and Mundy et al. 1986). Since uncertainties due to beam efficiencies and source couplings can affect the line ratios, the main beam efficiencies, accurate to about 10%, were verified on the planets. All such systematic calibration errors would shift all of the data points for a given transition together, and so would affect the relative line strengths, but not the radial distribution of emission in a given line. The source couplings to the main beam were taken into account by numerically convolving all of our model results for the globule with Gaussian beams of sizes equal to the observing beams. No small-scale clumping was included in the model because of the NH_3 results, which indicated an area-filling factor near unity.

4.1.1. *The Globule*

To perform the computations, the globule core data were first "symmetrized" by azimuthally averaging the observed intensities about the center of the globule. Thus we neglect the slight ellipticity seen in several of the CS line maps. In order to apply this procedure to the 5–4 data, the 5–4 map was first shifted by $(\Delta\alpha, \Delta\delta) = (9'', -3'')$ to line up its emission peak with that of the other three line maps. This symmetrized data set is plotted in Figure 7. The error bars on the off-axis points give the scatter between the individual points entering into this averaging process, while the error bars on the central points give an estimate of the systematic errors due to calibration. Toward the central position, the CS 2–1 and 3–2 lines are somewhat self-absorbed (Fig. 4*a*), and so provide only a lower limit to $T_{\rm MB}$. However, this applies only to the central position, as elsewhere the lower J lines do not appear obviously self-absorbed. The higher J lines show no self-absorption anywhere, but since optical depths for several of the lines may nevertheless be larger than 1 in the central region, we instead rely on the isotopic $C^{34}S$ transitions (which should be optically

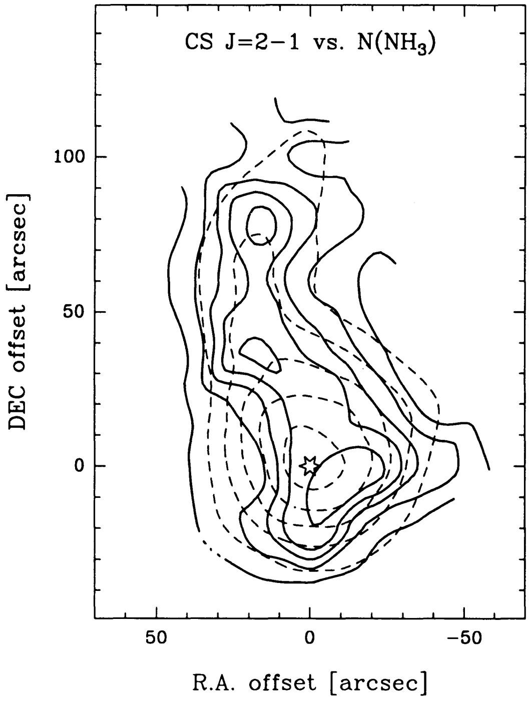

FIG. 6.—Overlay of the CS $J = 2$–1 line core map on the NH_3 column density map of Fig. 3*b*. Both sets of contours are at 30, 45, 60, 75, and 90% of the peak levels of their respective maps: 25 K km s^{-1} and 3×10^{14} cm^{-2}.

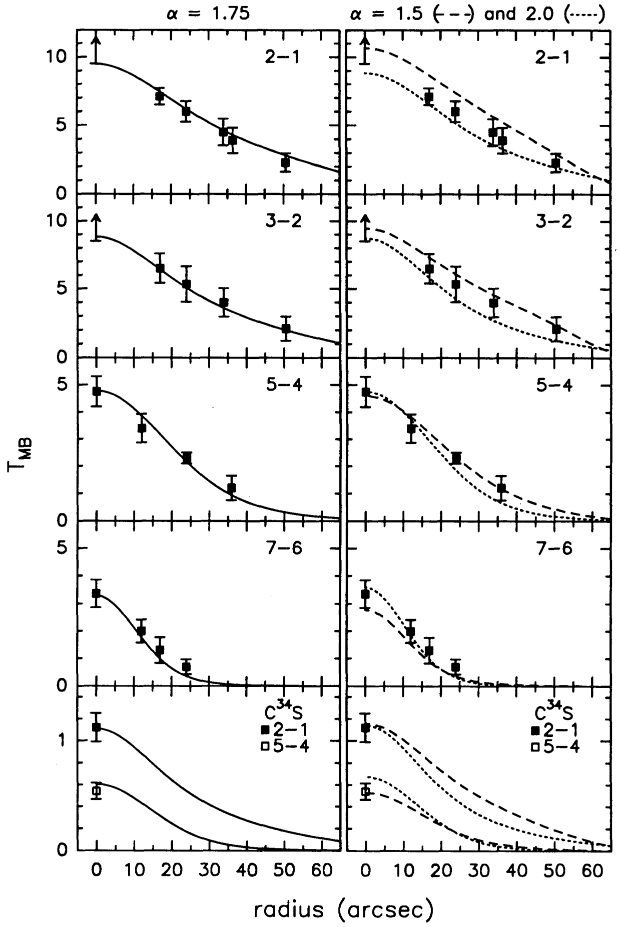

FIG. 7.—*Points:* symmetrized radial data set for CS and $C^{34}S$ main beam temperatures. The error bars for the on-axis points refer to systematic errors, and for the off-axis points to scatter in the azimuthal data sets. *Curves:* density power-law ($r^{-\alpha}$) model predictions for constant T ($=24$ K) and χ_{CS}. The models have been numerically convolved with Gaussian beams of the same FWHM as the observing beams. *Left:* best single-temperature model: $\alpha = 1.75$, $\chi_{CS} = 4.4 \times 10^{-10}$, $r_{max} = 0.29$ pc, $n_{H_2}(r_{max}) = 3.5 \times 10^4$ cm^{-3}, and mass 600 $M_{\odot}$. *Right:* two limiting models, with $\alpha = 1.5$ and 2. The former has $r_{max} = 0.22$ pc, $n_{H_2}(r_{max}) = 7 \times 10^4$ cm^{-3} and mass 570 $M_{\odot}$. The latter has $r_{max} = 0.29$ pc, $n_{H_2}(r_{max}) = 2 \times 10^4$ cm^{-3} and mass 360 $M_{\odot}$. Both have $\chi_{CS} = 5 \times 10^{-10}$.

thin) to determine the central column density, under the assumption $C^{32}S/C^{34}S = 23$.

The simplest molecular cloud model which could be applied is based on the large velocity gradient (LVG) assumption (Scoville & Solomon 1974; Goldreich & Kwan 1974; De Jong, Chu, & Dalgarno 1975) which calls for velocity differences across a molecular cloud which are much larger than the local line width, so that different parts of the cloud do not interact radiatively. Assuming homogeneous physical conditions, this allows for a "local" solution which also applies globally. Even if the physical conditions in the cloud are nonhomogeneous, as they are expected to be in IC 1396E, an LVG code can provide a useful first approximation to the line-of-sight averaged gas density. Based on only the observed ratio of the (presumably) optically thin $C^{34}S$ 5–4 and 2–1 lines, the resultant density is $\approx 8 \times 10^5$ cm^{-3}.

However, because the critical density for excitation of the observed CS transitions is a rapidly increasing function of J, and the temperature of the gas is rather uniform across the core of the globule, the observed decrease in source size with excitation state likely requires a steep radial density profile for the globule. The LVG assumption is thus not appropriate, and so more detailed calculations were carried out with a code based on the microturbulent assumption. In this case, the emission line shape is assumed the same throughout the cloud, and systematic motions small (Leung & Liszt 1976; White 1977), but the density and temperature are assumed to be functions of radius. All of these assumption appear appropriate to IC 1396E. The cloud models explored consisted of a number of spherically symmetric shells, spaced logarithmically in radius, out to a fixed maximum radius of r_{max}. The shell densities, temperatures, and abundances were assumed to follow power laws, with normalizations set at r_{max}. Initially, the number of shells was varied to determine if the solutions were converging; 30 were found to be sufficient. The collision rates used were $2^{1/2}$ times larger than the rates calculated for He by Green & Chapman (1978), to account for the lighter H_2 molecules.

The majority of the calculated models assumed constant temperature, T, and CS relative abundance, χ_{CS}, but in a small number of models, these were also varied. The assumption of fixed T follows from the uniformity of the NH_3 kinetic temperatures across the cloud core (20–23 K), and should be good except near the globule's outer periphery (§ 3), and near the embedded infrared source, where the far-infrared flux indicates a dust temperature of about 35 K in a small (7" diameter) volume (Walker et al. 1990; Wilking et al. 1989). Both of these effects serve to raise the gas temperature in small regions, which we partially compensate for in our calculations by assuming a constant $T = 24$ K, slightly higher than the observed range. As to the CS abundance, χ_{CS} might be affected by either of two factors—depletion onto grains at high densities near the globule core, and destruction by UV photons near the globule surface. However, both effects are highly uncertain, and so ignored.

As the first column in Figure 7 shows, for fixed T and χ_{CS}, all of the CS and $C^{34}S$ data in the symmetrized data set are very well fit by an $n_{H_2} \propto r^{-\alpha}$ density power law. The best solution shown is for $\alpha = 1.75$, $r_{max} = 9 \times 10^{17}$ cm, $n_{H_2}(r_{max}) = 3.5 \times 10^4$ cm^{-3}, and $\chi_{CS} = 4.4 \times 10^{-10}$. For a power-law distribution, the volume averaged density is $3/(3 - \alpha)$ times the outer density; hence $\alpha = 1.75$ implies $\langle n_{H_2} \rangle = 2.4 n_{H_2}(r_{max}) = 10^5$ cm^{-3}. In the central volume corresponding to the dust-core, this implies $\langle n_{H_2} \rangle = 2 \times 10^7$ cm^{-3}. These model globule parameters are summarized in Table 3.

The range of allowable exponents in the density power law was also examined. As the second column in Figure 7 shows, steeper power laws fall short of matching the full extent of the lower J emission without producing excessive 7–6 emission toward the cloud center, while less steep models produce the opposite effect: excessive low-J emission at large radii, which could be compensated for only within a limited range by reducing r_{max}. Thus, for the $\alpha = 1.5$ model shown, $r_{max} = 7 \times 10^{17}$ cm, while for the $\alpha = 1.75$ and 2.0 models, $r_{max} = 9 \times 10^{17}$ cm. The power law was thus found to be constrained by these factors to $r^{-1.75 \pm 0.2}$, the two extreme cases shown on the right half of Figure 7 being somewhat beyond these limits to make the noted effects more obvious. Note that the r_{max} range found, 7–9 × 10^{17} cm, very closely matches the globule's average optical radius.

Because of the presence of the embedded *IRAS* source, temperature effects also need to be explored briefly. To this end, a slight temperature gradient was added to the models, in order

TABLE 3

IC 1396E SOURCE AND MODEL PARAMETERS

Sizes and distances (pc):	
Source distance	750
Mean globule-ionization source separation	12.7
Globule R.A. radius (optical)	0.35
Globule declination radius	0.2
Velocities (km s^{-1}):	
Molecular FWHM line width	2.3
One dimensional velocity dispersion	1.0
Molecular sound speed (24 K)	0.3
Ionized sound speed (10^4 K)	11.4
Temperatures (K):	
Surface temperature	26
Inner temperature	20–23
Tail temperature	17
Density model for constant T (Fig. 7*a*):	
Outer radius, $r_{\max}$	0.29 pc
H_2 density	$3.5 \times 10^4 (r/r_{\max})^{-1.75}$ cm^{-3}
Derived globule parameters:	
Globule mass	$480 \pm 120\ M_\odot$
CS relative abundance, χ_{CS}	4.4×10^{-10}
NH_3 relative abundance, χ_{NH_3}	1×10^{-9}
H II region parameters:	
Lyman continuum rate of O6 star with Kurucz atmosphere	1×10^{49} s^{-1}
Incident flux, F_i	5.1×10^8 s^{-1} cm^{-2}
Reduction factor due to recombination layer	4
H II region surface ion density	74 cm^{-3}
Pressures ($/k$) at $r_{\max}$ (cm^{-3} K):	
Thermal, molecular	1×10^6
Ionization front	3.6×10^6
Turbulent, molecular	12×10^6

to produce a temperature rise toward the embedded *IRAS* source. With a 22 K outer temperature, and a power-law exponent of -0.1 (to match the average temperature of the small dust core), the emission in the 7–6 line, which arises mainly in a small central volume, increased by about 30% compared to our earlier "best" model. This extra emission could be counterbalanced by lowering the density exponent by about 0.15. The resultant $\alpha = 1.6$ model shown in Figure 8 (*left column*) is every bit as good as our earlier constant temperature model. The change in α called for by this "temperature gradient" model is not very large but suggests nonetheless that exponents just below our previously determined best α of 1.75 should be weighted more strongly than those above. Thus, an α in the range 1.55–1.75 is the most likely.

Additional observations of other CS and $C^{34}S$ lines might be thought capable of discriminating between the constant temperature and temperature gradient models. For other currently observable CS and $C^{34}S$ lines, the best constant temperature model solution (Fig. 7*a*) predicts the following main beam temperatures toward the cloud center: 1.9 K for $C^{34}S$ 3–2 at IRAM; and 0.3 K for $C^{34}S$ 7–6 and 0.6 K for CS 10–9 at the CSO. The temperature gradient model predicts a slightly lower 1.6 K for $C^{34}S$ 3–2; an identical $C^{34}S$ 7–6 intensity; and a CS 10–9 line higher by 40%, all relatively minor changes.

As a last check, the density and temperature were kept constant, but χ_{CS} was made a function of radius. This case is included primarily to illustrate the shortcomings of a single density solution. The best density exponent found above was thus blithely applied to χ_{CS} instead, while the density was in fact held constant. The result (Fig. 8, *right column*), as expected, shows that although the two $C^{34}S$ lines imply a density of roughly 7×10^5 cm^{-3}, very close to the initial LVG estimate, the CS 7–6 line is then by far too weak, and the other CS lines are too strong. Various tradeoffs can be made in which some lines fit more closely than others; however, no better overall solution is possible with a uniform density.

The total globule mass is given by the standard formula for a power-law density distribution,

$$M = \frac{4\pi m_H \mu_{H_2} r_{\max}^3 n_{H_2}(r_{\max})}{3 - \alpha}, \quad (1)$$

where m_H is the atomic mass of H, and $\mu_{H_2} = 2.8$ is the average mass per molecule, including He, in units of m_H. Note that M does not depend on χ_{CS}, but is very sensitive to the outer radius. For the estimated range of exponents, the mass is then roughly $480 \pm 120\ M_\odot$. Compared to other PIGs in H II regions which have been observed to date, this globule is on the heavy end of the spectrum (Nakano et al. 1989; Duvert et al. 1990; Cernicharo et al. 1992).

Integrating the NH_3 column density map of Figure 3 over the area of the CS cloud core, we derive an NH_3 abundance of roughly 10^{-9} in the globule core. Thus, both the NH_3 and CS abundances are somewhat low (e.g., Menten et al. 1987; Schulz et al. 1991; Zhou et al. 1991). This, together with the conclusion that the globule is externally heated, suggests that external UV photons are responsible for both heating and molecular dissociation throughout the globule, which in turn requires a clumpy medium (which could lower the mass estimate). However, as discussed earlier, the NH_3 *area*-filling factor must nevertheless be near unity, and so must that of CS, since the observed line temperatures are quite high, compared to both T_K and the excitation temperatures.

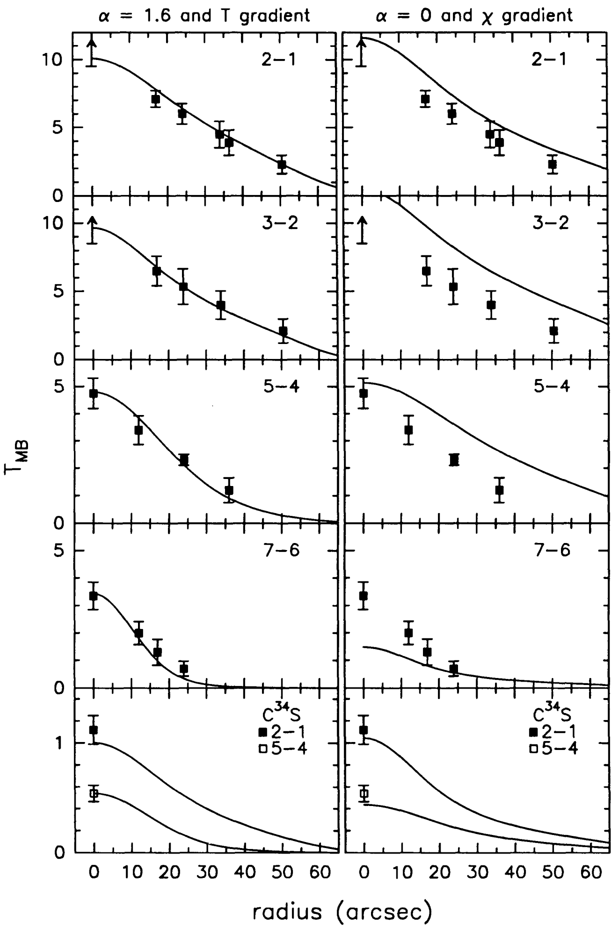

FIG. 8.—*Points*: same as Fig. 7. *Curves*: *Left*: best model with $T \propto r^{-0.1}$. Other parameters: $\alpha = 1.6$, $\chi_{CS} = 4.6 \times 10^{-10}$, $r_{max} = 0.22$ pc, $T(r_{max}) = 22$ K, $n_{H_2}(r_{max}) = 6 \times 10^4$ cm^{-3} and mass 480 $M_\odot$. *Right*: model with constant T and n_{H_2}, but $\chi_{CS} \propto r^{-1.75}$.

4.1.2. *Comparison with Previous Mass Determinations*

The resultant globule mass of 480 $M_\odot$ is roughly a factor of 3 larger than the 150 $M_\odot$ deduced for this globule from observations of the ^{13}CO 1–0 line (Sugitani et al. 1989). The authors present insufficient detail to further investigate the nature of this difference, but we note that the CS estimate is based on local densities and does not depend on assumed molecular abundances.

The derived mass also exceeds by roughly a factor of 50 the mass deduced for the FIR continuum-emitting region around IRAS 21391+5802 (7–11 $M_\odot$; Walker et al. 1990; Wilking et al. 1989), which however refers to a much smaller volume (7″ diameter = 0.025 pc). Dust emission from the full volume of the globule is not more prominent because the optically thin dust continuum emission is proportional to both column density and temperature, and so is a sharply peaked function, requiring a much larger dynamic range than the extant continuum observations possess. However, in the same 7″ diameter volume, our $\alpha = 1.75$ density law predicts a mass of 23 $M_\odot$, only a factor of 2 above that estimated from the dust continuum observations, and so there is reasonable agreement, within the uncertainties. If the temperature gradient model is considered instead, the agreement is even better, as the flatter density law moves more of the mass out to larger radii, leaving only 15 $M_\odot$ in the central volume.

4.1.3. *The Tail*

Along the tail north of the main globule, the temperature of the gas (17 K) is known from the NH$_3$ observations, but the only CS data available are the 3–2 and 2–1 intensities. These show a (3–2)/(2–1) line ratio of roughly 0.6 ± 0.1, when averaged over the tail (no beam coupling correction to this ratio was attempted because of the sparse sampling in this region). Since no C^{34}S line was observed toward the tail, the line opacities are unknown, but the low opacity limit implies an average density of $10^{5.2\pm0.2}$ cm^{-3}. However, the observed main beam temperatures of roughly 5 K and 3 K for the 2–1 and 3–2 lines, respectively, imply opacities of order unity, and densities lower than this by a factor of up to about 2.

4.1.4. *The Line Wings*

The line wings were detected in all four of the CS lines observed, but in neither of the isotopically substituted C^{34}S lines, implying an upper limit to the CS 5–4 line opacity of ≈ 2. For comparison purposes, the CS spectra in each of the lines were first smoothed to the same 29″ beam. The intensities of the three lowest transitions are then comparable, but the 7–6 line is weaker than the 5–4 line by about a factor of 2. Because the gas temperature is unknown, the density estimate is somewhat uncertain, but making the reasonable assumption that the gas temperature lies between 25 and 100 K, the 7–6 to 5–4 ratio implies densities of 2×10^7 to 1×10^6 cm^{-3}.

5. DISCUSSION

The presence of an infrared source of some 300 $L_\odot$ and an associated molecular outflow near the core of IC 1396E (Sugitani et al. 1989; Wilking et al. 1989; Walker et al. 1990) indicates that star formation has recently occurred in this globule. (Since the globule mass is several hundred $M_\odot$, the stellar mass is a small fraction of the total.) The globule should thus show signs of instability to collapse, and indeed radial density distributions of $r^{-1.55}$ to $r^{-1.75}$ are not equilibrium solutions of Poisson's equation. They are, however, close to the density distribution predicted by the $n \propto r^{-1.5}$ collapse model of Shu (1977). In particular, the model with a slight temperature gradient is quite close. Taking for granted that the globule is unstable, the question then becomes whether the collapse was initiated spontaneously, through the action of the globule's own gravity, or externally, via the ionization front (IF). Since the cloud's density peak occurs quite distant from the IF, the shock wave which might accompany the ionization front (e.g., Kahn 1954) cannot be responsible for its existence. However, while the existence of a steep density profile in the molecular clump must thus predate the arrival of the IF, its collapse might nonetheless have been triggered by the external perturbation. We turn now to a closer examination of this question.

The pressure forces acting on the globule include the thermal and turbulent pressures of the molecular gas, and the pressure of the ionized boundary layer (IBL). Since the IBL is thin compared to the globule radius, the advance of the ionization front into the globule can be analyzed in terms of a relatively simple model (e.g., Spitzer 1978), in which the newly evaporated ions are assumed to stream off the spherical globule surface at roughly the isothermal sound speed, c_i, yielding an ion density outside the globule which is proportional to r^{-2}. The total number flux of ions leaving the globule surface is equal to the photon flux, F, reaching the molecular boundary. Because of recombinations in the IBL, F is reduced from the incident flux, F_i, by a factor which is roughly 6 in this simple treatment. The value of F_i used was that of an O6 star with a Kurucz (1979) atmosphere (see Güsten & Mezger 1982). The ion density at the globule surface, n_i, is then $n_i = F/c_i$, and the pressure on the globule is roughly $P_i = 4FT_i/c_i$, where T_i is the ionized gas temperature, and the factor of 4 accounts for both the thermal and ram pressures of the ions and electrons. For $T_i = 10^4$ K, we have $P_i/k \approx 3 \times 10^6$ cm^{-3} K. A more exact treatment of the IBL (Bertoldi 1989; Bertoldi & McKee 1990) gives results very similar to these, the reduction in incident flux being a factor of 4, and $P_i/k = 3.6 \times 10^6$ cm^{-3}. These numerical values are summarized in Table 3.

In comparison (using the parameters of the best single-temperature model of Fig. 7), the internal pressure (divided by k) at $r_{\max}$ consists of 1×10^6 cm^{-3} K of thermal pressure, and a much larger turbulent pressure of 1.2×10^7 cm^{-3} K (using $P = \rho a^2$, with ρ the gas density and a the turbulent velocity dispersion). The latter exceeds the external pressure by a factor $\gtrsim 3$, large enough to be on the edge of significance (note that the temperature gradient model [Fig. 8] has an even larger internal pressure at $r_{\max}$). The uncertainties in determining the ionized gas pressure arise primarily in the incident flux, while the uncertainties in the internal pressure arise from the H_2 collision rates, our assumption that a single power law adequately describes the entire globule, and the lack of knowledge concerning the nature of the turbulence (if the cloud consists of numerous small, dense clumplets which move supersonically in a less dense medium, the interclump medium might be in pressure balance with the external H II region pressure). Furthermore, this pressure imbalance will grow with time as the ionization front eats its way into the cloud, since the external pressure at the globule's surface is fixed by the incident flux and cloud radius (Bertoldi & McKee 1990), and can rise only as $r_{\max}^{-0.5}$, while the internal pressure at the cloud edge will rise much more rapidly, due primarily to the much steeper rise in molecular density inward. This pressure structure is shown in Figure 9. Thus, even allowing for uncertainties, it is reasonable to conclude that the globule is not contained by the pressure of the ionization front, but rather by its own internal gravity.

The external pressure determines the maximum interior mass which is stable against collapse, according to the Bonner-Ebert relation (Bonner 1956; Ebert 1955). For the calculated external pressure and internal turbulent velocity width, this limiting mass is $\approx 170\ M_\odot$, less than the measured mass. The virial theorem calls for a mass of $\approx 330\ M_\odot$, also smaller than the observed mass, but not significantly so. Since a rotation sufficiently large to support the cloud ($v_{\rm rot} > 2.6$ km s^{-1} at the cloud edge) is not observed, and magnetic fields of several hundred μG would be required for support, all indications are that the cloud must be unstable to collapse, as pointed out earlier. Although the uncertainties involved provide a bound to the certainty of this conclusion, the presence of a central star makes the point moot. However, the observed line widths are by far too small for free-fall collapse ($v \approx 3.8$ km s^{-1}) to be occurring throughout the cloud, and furthermore, the lack of redshifted self-absorption in the spectra directly precludes free-fall. On the other hand, based on the observed turbulent velocity dispersion of IC 1396E and the estimated globule mass and radius, the self-similar collapse model of Shu (1977) predicts an infall velocity of only 0.1 km s^{-1}. Such a slow collapse is fully consistent both with the observed line shapes, and with the microturbulent assumption on which the radiative transfer calculations were based, since this calls for systematic motions small compared to the turbulent line width. (Of course, very near the cloud center, where both the central star and the broad line wings are seen, systematic motions may indeed dominate.)

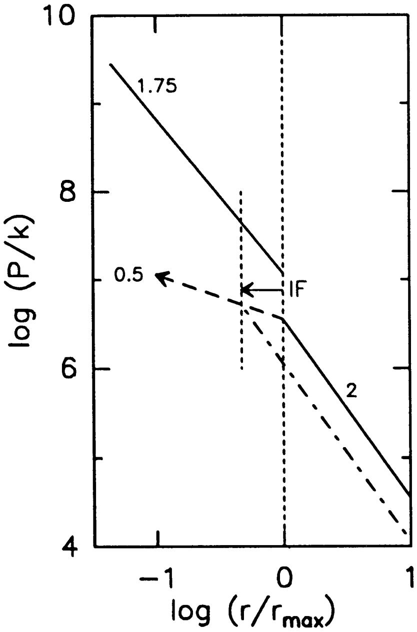

FIG. 9.—Pressure distribution vs. radius for the symmetrized globule. The current ionization front (IF) is denoted by the dotted vertical line at $r_{\max}$, and the solid lines show the current pressure distribution in the molecular globule and its ionized envelope. The associated exponents of the $r^{-\alpha}$ power laws are indicated ($\alpha = 1.75$ and 2, respectively). The rest of the curves refer to the globule's later evolution. The dashed curve shows the evolution of the ionized pressure at the surface of the globule as the radius decreases ($r_{\max}^{-0.5}$). The location of the IF, for an arbitrary later time, is indicated by the smaller vertical dashed line. At this time, the pressure in the ionized gas is given by the dash-dotted curve, and the pressure interior to the globule by the solid curve to the left of the smaller vertical line.

Returning now to the ionization front, the high gas density observed implies that the ionization front can advance into the cloud only very slowly. Naively, its velocity would be $u_{\rm IF} = F/\mu_i n_{\rm H_2} = 17$ m s^{-1}. Here μ_i is the number of ions produced per H_2 molecule ($=2.2$). However in a dense medium, $u_{\rm IF}$ cannot exceed the D-critical velocity ($u_D = c_0^2/2c_i \approx 4$ m s^{-1}, where c_0 is the isothermal sound speed in the molecular medium) without generating a shock wave which precompresses the medium ahead of the IF so that $u_{\rm IF} \approx u_D$ (Kahn 1954; Spitzer 1978; Osterbrock 1989). The resultant shock velocity would be (Bertoldi 1989, with minor modifications for a molecular medium)

$$v_{\rm sh} = \sqrt{\frac{2\mu_{\rm H\,II} c_i F}{\mu_{\rm H_2} n_{\rm H_2}}}\,, \tag{2}$$

where $\mu_{\rm H\,II}(=1.27)$ is the average mass per nucleus in the H II region, in units of $m_{\rm H}$. With $n_{\rm H_2} = n_{\rm H_2}(r_{\max})$, the reduced photon flux yields $v_{\rm sh} \approx 0.6$ km s^{-1}, only twice c_0. Such a weak shock cannot be very effective at compressing the gas. Given also the low $u_{\rm IF}$ and mass ablation rate ($\dot{M} = 7 \times 10^{-6}\ M_\odot$ yr^{-1}), the current configuration of the ionization front is then nearly stationary, and long-lived compared to the lifetime of an O6 star.

The rise in density toward the interior of the globule reduces the effectiveness of the shock wave even further. Conservation of momentum yields a shock speed inversely proportional to the square root of the density (eq. [2]), implying a slowing of the shock as it advances toward the core. For the measured cloud parameters, v_{sh} drops to c_0, and the compression to insignificance, at a radius $\approx r_{max}/2$. Thus, the density profile in the central core of the globule should not be altered markedly by the ionization front.

There is one further wrinkle. If, as concluded earlier, the external pressure is indeed lower than the internal pressure, subcritical *D*-type conditions should apply, and no shock should *currently* be generated. As discussed above, the subcritical requirement does not seem to be satisfied with the measured cloud parameters. However, if u_D is calculated from the observed one-dimensional turbulent line width rather than from the isothermal sound speed, we find instead $u_{D,\rm turb} = a^2/2c_i \approx 44$ m s^{-1}, which exceeds $u_{\rm IF}$, and so subcritical conditions would apply. For this modification to be applicable, the turbulence must extend to small enough scales so that $P = a\rho$, instead of the usual thermal relation $P = c_0 \rho$, an assumption of unknown, but dubious, validity. Nevertheless, the consistency between a lower external pressure and lack of a shock wave has attractions.

In either case, the main conclusion is that the ionization front is *currently* not able to drive a strong shock into the IC 1396E globule. This is not to say that a shock was not generated sometime in the past, when the ionization front first reached the globule's former lower density envelope. However, even so, the shock would still slow toward the cloud core, and the compression would lose effectiveness. Thus, while gas which may have existed beyond the boundaries of the currently observed PIG could have been compressed to a more significant extent, the dense core of the cloud cannot have been directly compressed much. This suggests a modest flattening of the outer parts of the preexisting density profile may have occurred, and so it is possible to speculate that the initial cloud density profile may have been closer to r^{-2}, the solution for a singular isothermal sphere.

This being the case, could the compression of the outer layers of the cloud and the subsequent communication of this new outer density distribution to the core have initiated the core collapse, by perturbing the core slightly from an equilibrium distribution? Certainly this is a possibility, since the sound and turbulence crossing times (10^6 and 3×10^5 yr, respectively) are both small compared to the lifetime of the O6 exciting star (4–5×10^6 yr) and the evaporation timescale (6×10^7 yr), but larger than or comparable to the free-fall time of 2×10^5 yr. However, since the dense globule core could not have been directly compressed by the ionization front, and is well separated from it, the globule must have evolved to nearly the observed degree of central condensation on its own. Thus, the globule must have been predisposed to collapse, and was already evolving toward collapse on its own. Indeed, power-law distributions such as the one observed for this globule are known to occur during the normal evolution and collapse of molecular cloudlets (Lizano & Shu 1989). Thus, given that an ionization front is innocent until proven guilty, and that the globule itself was already predisposed to collapse, the evidence for ionization front–driven collapse appears at best to be circumstantial. As a working hypothesis, the star formation in this PIG is therefore best viewed as a case of spontaneous collapse.

6. CONCLUSIONS

IC 1396E is an almost textbook example of an externally heated, centrally condensed molecular globule. Even though an internal infrared energy source is present, the bulk of the globule's volume appears to be heated by the external ultraviolet radiation from the cluster ionizing IC 1396. The density profile of the globule is steep, $r^{-1.55}$ to $r^{-1.75}$ for an assumed constant temperature profile. The densest gas is near IRAS 21391+5802, well away from the ionization front. Because of the density falloff toward the ionization front, the globule IC 1396E appears to be a preexisting density enhancement which has survived the destruction of the molecular cloud by virtue of its high density. No noncircumstantial evidence for ionization front triggered collapse is found.

We wish to thank the technical staffs of the IRAM 30 m and CSO 10.4 m telescopes for help in acquiring the data; F. Bertoldi, P. Goldreich, F. Shu, D. van Buren, C. Walker, & B. Wilking for helpful comments and discussions; and an anonymous referee for his comments and porcine poetry. Particular thanks go to N. Reid for supplying the Palomar Plate from the second survey and for measuring the stellar coordinates. We also acknowledge support from NATO grant 0809/87 and NSF grant AST 90-15132.

Part of this work is based on photographic plates obtained at the Palomar Observatory 48 inch Oschin Telescope for the Second Palomar Observatory Sky Survey which was funded by the National Geographic Society, the Eastman Kodak Company, the Alfred Sloan Foundation, the Samuel Oschin Foundation, NSF grants AST 84-08225 and AST 87-19465, and NASA grants NGL 05002140 and NAGW 1710.

REFERENCES

Bertoldi, F. 1989, ApJ, 346, 735
Bertoldi, F., & McKee, C. F. 1990, ApJ, 354, 529
Bonner, W. B. 1956, MNRAS, 116, 351
Cernicharo, J. 1991, in The Physics of Star Formation and Early Stellar Evolution, ed. C. J. Lada & N. D. Kylafis (Dordrecht: Kluwer), 287
Cernicharo, J., Bachiller, R., Duvent, G., Gonzalez-Alfonso, E., & Gomez-Gonzalez, J. 1992, A&A, 261, 589
Danby, G., Flower, D. R., Valiron, P., Schilke, P., & Walmsley, C. M. 1988, MNRAS, 235, 229
De Jong, T., Chu, S.-I., & Dalgarno, A. 1975, ApJ, 199, 69
Duvert, G., Cernicharo, J., Bachiller, R., & Gomez-Gonzalez, J. 1990, A&A, 233, 190
Ebert, R. 1955, Z. Astrophys., 37, 217
Green, S., & Chapman, S. 1978, ApJS, 37, 16
Goldreich, P., & Kwan, J. 1974, ApJ, 189, 441
Güsten, R., & Mezger, P. G. 1982, Vistas Astron., 26, 159
Kahn, F. D. 1954, Bull. Astron. Inst. Netherlands, 12, 187
Kurucz, R. L. 1979, ApJS, 40, 1
Leung, C. M. 1985, in Protostars and Planets II, ed. D. C. Black & M. S. Matthews (Tucson: Univ. of Arizona Press), 104
Leung, C. M., & Liszt, H. S. 1976, ApJ, 208, 732
Liszt, H. S., & Leung, C. M. 1977, ApJ, 218, 396
Lizano, S., & Shu, F. H. 1989, ApJ, 342, 834
Matthews, H. E. 1979, A&A, 75, 345
Menten, K., Serabyn, E., Güsten, R., & Wilson, T. L. 1987, A&A, 177, L57
Mundy, L., Snell, R. L., Evans, N. J., II, Goldsmith, P. F., & Bally, J. 1986, ApJ, 306, 670
Nakano, M., Tomita, Y., Ohtani, H., Ogura, K., & Sofue, Y. 1989, PASJ, 41, 1073
Osterbrock, D. E. 1989, Astrophysics of Gaseous Nebulae and Active Galactic Nuclei (Mill Valley, CA: University Science Books), 177
Pauls, T. A., Wilson, T. L., Bieging, J. H., & Martin, R. N. 1983, A&A, 124, 23

Pottasch, S. 1956, Bull. Astron. Inst. Netherlands, 13, 77
Schulz, A., Güsten, R., Zylka, R., & Serabyn, E. 1991, A&A, 246, 570
Schwartz, R. D., Gyulbudaghian, A. L., & Wilking, B. A. 1991, ApJ, 370, 263
Scoville, N. Z., & Solomon, P. M. 1974, ApJ, 187, L67
Shu, F. H. 1977, ApJ, 214, 488
Shu, F. H., Adams, F. C., & Lizano, S. 1987, ARA&A, 25, 23
Simonson, S. C., III, 1968, ApJ, 154, 923
Snell, R. L., Langer, W. D., & Frerking, M. A. 1982, ApJ, 255, 149
Snell, R. L., Mundy, L. G., Goldsmith, P. F., Evans, N. J., II, & Erickson, N. R. 1984, ApJ, 276, 625
Spitzer, L. 1978, Physical Processes in the Interstellar Medium (New York: Wiley)
Sugitani, K., Fukui, Y., Mizuno, A., & Ohashi, N. 1989, ApJ, 342, L87
Tereby, S., Shu, F. H., & Cassen, P. 1984, ApJ, 286, 529
Walker, C. K., Adams, F. C., & Lada, C. J. 1990, ApJ, 349, 515
Wendker, H. J., & Baars, J. W. M. 1980, A&A, 89, 180
White, R. E. 1977, ApJ, 211, 744
Wilking, B., Blackwell, J. H., & Mundy, L. G. 1990, AJ, 100, 758
Wilking, B., Mundy, L. G., Blackwell, J. H., & Howe, J. E. 1989, ApJ, 345, 257
Zhou, S., Evans, N. J., II, Güsten, R., Mundy, L., & Kutner, M. 1991, ApJ, 372, 518.